NANO LETTERS

pubs.acs.org/NanoLett

Letter

Modulating Charge-Density Wave Order and Superconductivity from Two Alternative Stacked Monolayers in a Bulk 4*Hb*-$TaSe_2$ Heterostructure via Pressure

Limin Yan, Chi Ding, Mingtao Li, Ruilian Tang, Wan Chen, Bingyan Liu, Kejun Bu, Tianheng Huang, Dongzhe Dai, Xiaobo Jin, Xiaofan Yang, Erjian Cheng, Nana Li, Qian Zhang, Fengliang Liu, Xuqiang Liu, Dongzhou Zhang, Shuailing Ma, Qiang Tao, Pinwen Zhu, Shiyan Li, Xujie Lü, Jian Sun,* Xin Wang,* and Wenge Yang*

Cite This: *Nano Lett.* 2023, 23, 2121−2128

Read Online

ACCESS | Metrics & More | Article Recommendations | Supporting Information

ABSTRACT: Two-dimensional (2D) van der Waals heterostructures (VDWHs) containing a charge-density wave (CDW) and superconductivity (SC) have revealed rich tunability in their properties, which provide a new route for optimizing their novel exotic states. The interaction between SC and CDW is critical to its properties; however, understanding this interaction within VDWHs is very limited. A comprehensive in situ study and theoretical calculation on bulk 4*Hb*-$TaSe_2$ VDWHs consisting of alternately stacking 1*T*-$TaSe_2$ and 1*H*-$TaSe_2$ monolayers are investigated under high pressure. Surprisingly, the superconductivity competes with the intralayer and adjacent-layer CDW order in 4*Hb*-$TaSe_2$, which results in substantially and continually boosted superconductivity under compression. Upon total suppression of the CDW, the superconductivity in the individual layers responds differently to the charge transfer. Our results provide an excellent method to efficiently tune the interplay between SC and CDW in VDWHs and a new avenue for designing materials with tailored properties.

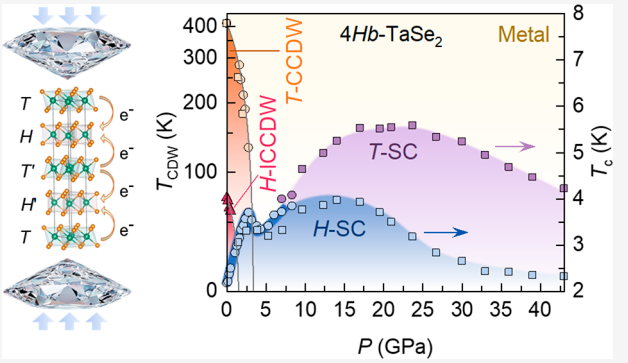

KEYWORDS: *2D materials, charge-density wave, superconductivity, bulk van der Waals heterostructure, charge transfer, high pressure, $TaSe_2$*

Two-dimensional (2D) van der Waals heterostructures (VDWHs)[1−3] have attracted great interest in the past decade, especially for improving their emerging properties as multifunctional devices and determining their fundamental mechanisms. Metallic 2D transition-metal dichalcogenide (TMD) VDWHs that possess charge-density wave (CDW) states and superconductivity (SC) have recently attracted tremendous attention for their highly modulated CDW orders and superconductivity,[4−8] showing huge potential for multifunctional devices with practical applications. More interestingly, many theoretical and experimental studies have demonstrated that the CDW orders involved in the displacements are not only from the in-plane metallic atoms but also from the out-of-plane chalcogen atoms,[9,10] which may largely modulate the properties of adjacent components when fabricating them into VDWHs. Furthermore, it is well-known that the modulation of the CDW states through chemical or physical tuning tools commonly glues the superconducting properties,[11−19] in that both of them originate from the instability of the Fermi surface and electron−phonon coupling (EPC).

However, the studies of electronic properties induced by the CDW order, such as Mott insulating states[20] and "better (or poor)" conductor behavior,[21] and the relationship (e.g., coexisting, competing, or cooperating)[11−19] between CDW and superconductivity within VDWHs are still limited. Furthermore, although a few successful cases have tuned the electrical-transport properties on 2D-limit layered materials, such as trilayer graphene in a diamond anvil cell,[22] the wide-range applications of this technique to 2D VDWHs are still technically challenging. Addressing these problems requires suitable material systems in combination with advanced regulation and diagnostic tools that could enable the fine tuning of the layered interaction and in situ characterization of

Received: November 7, 2022
Revised: February 26, 2023
Published: March 6, 2023

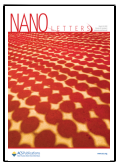

https://doi.org/10.1021/acs.nanolett.2c04385
Nano Lett. 2023, 23, 2121−2128

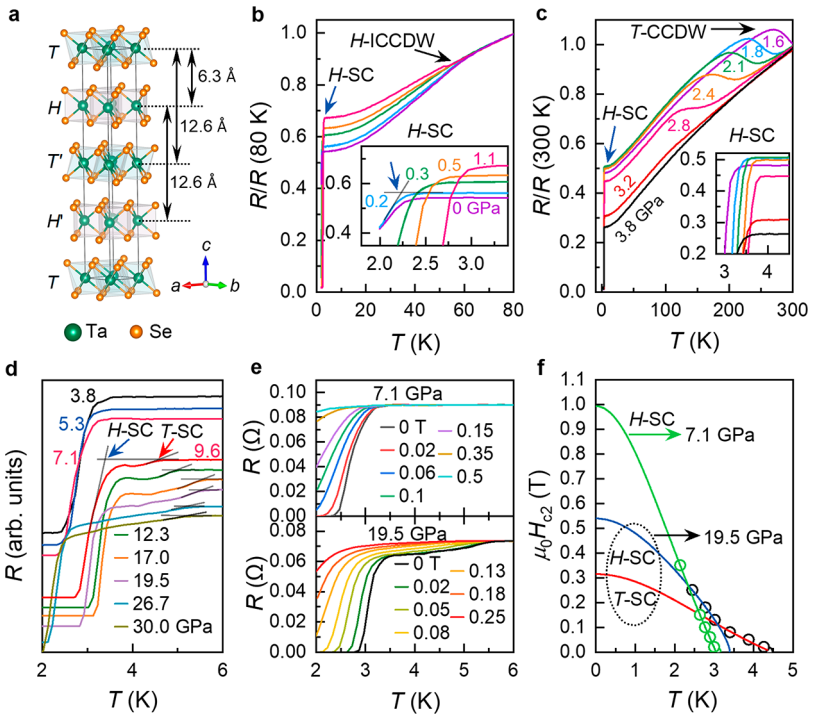

Figure 1. Crystal structure and high-pressure electrical transport measurements of bulk 4*Hb*-$TaSe_2$. (a) Crystal structure of 4*Hb*-$TaSe_2$ under ambient conditions. (b–d) Selected $R(T)$ profiles at different pressures: 0 GPa ≤ P ≤ 1.1 GPa (run 1), 1.6 GPa ≤ P ≤ 3.8 GPa (run 1), and 3.8 GPa ≤ P ≤ 30.0 GPa (run 2), respectively. The criteria for determining T_c are indicated in (b) and (d) as the intersection point of the two extrapolated $R(T)$ straight lines. Insets in (b) and (c) present an enlarged view of the pressure-boosted T_c in the H-layer. (e) $R(T)$ profiles at different magnetic fields for 7.1 GPa (top) and 19.5 GPa (bottom). (f) Temperature-dependent upper critical field $\mu_0 H_{c2}$ at 7.1 and 19.5 GPa. The solid lines represent the Ginzburg–Landau (GL) fittings.[35] Here, T_c is defined by the resistance criterion R_c = 90% R_n, where R_n is the normal state resistance just above its drop.

the electrical-transport properties. Recently, the emerging natural bulk TMD VDWHs that share configurations similar to those of 2D VDWHs are ideal systems suitable for such studies. They are alternately stacked with octahedral (T) layers with CDW order and trigonal-prismatic (H) layers with superconductivity and different CDW orders.[23−27] Pressure is a clean, continuous, and reversible way to regulate the interlayer coupling by changing the interlayer distance without introducing any chemical impurities into VDWHs.[28,29] Pressure has also been broadly applied in bulk TMD systems to tune the electronic properties associated with the CDW states and superconductivity.[11−19]

Here, we synthesized a 4*Hb*-$TaSe_2$ single crystal, which is alternately stacked by the T-layer and H-layer $TaSe_2$ (see synthesis details in the Method section and characterizations in Figure S1 in the Supporting Information). At ambient pressure, we observed H-layer superconductivity (T_c ≈ 2.2 K) and two electrical transport signatures induced by CDW transitions from the H-layer (at ∼73 K) and T-layer (at ∼410 K). By applying pressure, the superconductivity of the H-layer can be boosted by the suppression of the H-layer CDW, as well as the T-layer CDW due to the three-dimensional nature of the T-layer CDW. More interestingly, when the CDW states are suppressed by pressure, the dual-layer superconductivity (from H-layer and T-layer) starts to appear at 9.6 GPa. Compared to the bulk counterparts, the superconductivity of the H-layer is more sensitive to charge transfer than the T-layer due to different electronic band structures.

Structurally, alternately stacking 1T-$TaSe_2$ and 1H-$TaSe_2$ monolayers yield the natural heterogeneous 4*Hb*-$TaSe_2$ phase with a space group $P6_3/mmc$ hexagonal symmetry (Figure 1a).[30] Compared with the bulk 1T- or 2H-$TaSe_2$ structure (Figure S2), the doubled distance along the stacking direction (c axis) between the adjacent H–H or T–T layers significantly weakens the interlayer coupling. As a consequence, the electronic band structures of monolayer 1T- and 1H-$TaSe_2$ are relatively well-preserved within 4*Hb*-$TaSe_2$ (Figure S3). At ambient pressure, the observed T_c of bulk 4*Hb*-$TaSe_2$ at 2.2 K (Figure 1b) is in line with the theoretical prediction from monolayer 1H-$TaSe_2$ (∼2.2 K),[31] but it shows a significant enhancement compared to the bulk 2H-$TaSe_2$ (∼0.2 K).[32] To the best of our knowledge, this is the first observation of a superconducting transition in 4*Hb*-$TaSe_2$. A similar enhancement of superconductivity has also been reported in similar structures of 4*Hb*-TaS_2 and 6R-TaS_2 very recently.[23−25,27] Furthermore, the magnetic anisotropy of 4*Hb*-$TaSe_2$ is characterized by the upper critical field in-plane ($H_{c2}^{\parallel}$) to out-of-plane ($H_{c2}^{\perp}$) ($H_{c2}^{\parallel}/H_{c2}^{\perp}$ = 7.5) ratio, which is significantly enhanced by about 3 times compared to the bulk 2H-$TaSe_2$.[33] The details can be found in Figure S4. As shown in Figure 1b, the rapid drop in the $R(T)$ curve at ∼73 K indicates that the H-layer enters into the incommensurate CDW (ICCDW) state,[34] while the sudden increase in resistance is contributed by the commensurate CDW (CCDW) in the T-layer (∼410 K at ambient pressure; see Figure S4a) as shown in Figure 1c. Here, the transition temperature of the CCDW (T_{CCDW}^{T}) for the T-layer and ICCDW (T_{ICCDW}^{H}) for the H-layer are determined by the minimum value of dR/dT and the deflection point (shown in the insets of Figure S4a,b), respectively.

https://doi.org/10.1021/acs.nanolett.2c04385
Nano Lett. 2023, 23, 2121−2128

To investigate the interplay between the SC and CDW states with pressure in 4*Hb*-$TaSe_2$, we conducted in situ high-pressure electrical transport measurements on single-crystal flakes between 2 and 300 K. Two independent runs were performed with different pressure-transmitting media (PTM): run 1 with NaCl powder for 0 GPa $\leq P \leq$ 9.3 GPa and run 2 with silicone oil for 1.5 GPa $\leq P \leq$ 43.0 GPa. The complete $R(T)$ profiles, including both cooling and warming processes, can be found in Figure S5. The criteria for determining T_{CDW} at various pressures are shown in Figure S6. As shown in Figure 1b,c, the signature of the ICCDW (CCDW) state in the *H*-layer (*T*-layer) cannot be identified from the $R(T)$ curves above 1.1 GPa (3.2 GPa). Interestingly, T_c initially increases accompanied by the suppression of ICCDW in the *H*-layer below 1.1 GPa. However, it continuously increases concomitantly with the suppression of the CCDW in the *T*-layer and reaches a maximum value of 3.7 K at 2.8 GPa (the inset of Figure 1c) where the CCDW is largely suppressed, and then it decreases until 5.3 GPa (Figure 1d). Remarkably, at 9.6 GPa and above, the resistance slightly drops first, followed by a fast drop and its onset temperature varies with pressure, which indicates that a new superconducting transition occurred in the 4*Hb*-$TaSe_2$ sample. A high-pressure structural analysis and first-principles calculations support that the emergent superconductivity with a higher T_c originates from the *T*-layer. Figure 1e displays the $R(T)$ curves at different magnetic fields for 7.1 and 19.5 GPa, and the corresponding $\mu_0 H_{c2}$ as a function of the critical temperature T_c is given in Figure 1f. In contrast to a single temperature (T)−magnetic field (H) profile at 7.1 GPa, the $T-H$ profile at 19.5 GPa can be divided into two parts, indicating that two superconducting states coexist. By fitting the $\mu_0 H_{c2}(T)$ with the GL equation, the zero-temperature $\mu_0 H_{c2}(0)$ of the *H*-layer and *T*-layer can be estimated to be ∼0.53 and ∼0.32 T, respectively. Herein, we call the two superconducting transitions emerging from two distinguished layers "dual-layer superconductivity".

Figure 2a summarizes the CDW and SC transition temperatures vs the pressure of 4*Hb*-$TaSe_2$. We found that both CDW states from the *H*- and *T*-layers follow a mean-field power law,[36] $T_{CDW}(P) = T_0(1 - P/P_c)^{\beta}$, where T_0 is the transition temperature of the CDW state at ambient pressure and β is an exponential parameter. For the *H*-layer (T_0 = 73 K), T^{H}_{ICCDW} falls rapidly as $(1 - P/P_c)^{0.5}$ with pressure, yielding P_c = 1.4 GPa. Elastic neutron scattering on 4*Hb*-$TaSe_2$ did not find any hint of CCDW down to 10 K.[34] Freitas et al. reported that the transition temperature of ICCDW of bulk 2*H*-$TaSe_2$ (T^{2H}_{ICCDW}) was first suppressed at ∼4.4 GPa, followed by the reentry of CCDW, and survived until 20 GPa,[15] while Chu et al. reported the CCDW transition temperature of bulk 2*H*-$TaSe_2$ (T^{2H}_{CCDW}) as ∼1.7 GPa.[37] For the *T*-layer (T_0 = 410 K), the critical P_c = 3.32(1) GPa is almost half of that in bulk 1*T*-$TaSe_2$, and the exponential parameter β = 0.62(2) is slightly higher than that of bulk 1*T*-$TaSe_2$.[16] We further analyzed the $R(T)$ curves of the normal state with the empirical formula $R(T) = R_0 + A \cdot T^n$ at $T_c < T \leq$ 30 K. Here, R_0 is the residual resistance contributed from impurity scattering, A is a prefactor, and n is the exponential parameter. $n(P)$ (Figure 2b, left) forms a dip accompanied by a peak in $A(P)$ (Figure 2b, right) at ∼2.5 GPa, while the first dome-like *H*-layer's $T_c(P)$ is also centered near this pressure. All these suggest the scenario of quantum fluctuation induced by the suppression of the CDW state in the TMD system.[14,16,18] However, the situation in 4*Hb*-$TaSe_2$ is more complicated. The first

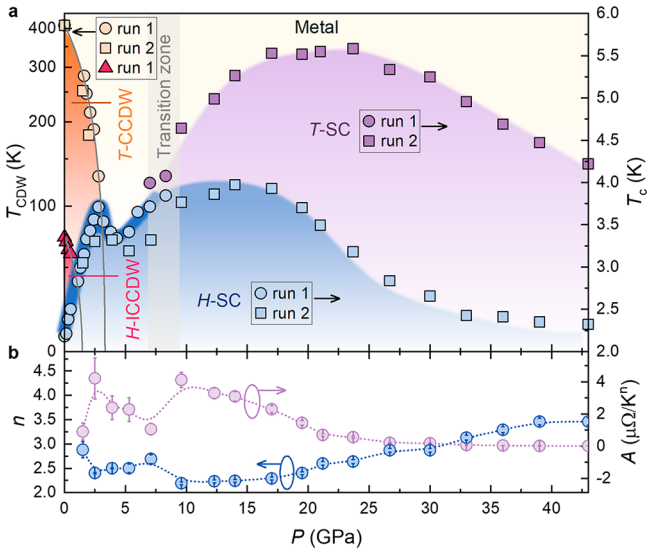

Figure 2. T_{CDW} and T_c vs P diagrams of 4*Hb*-$TaSe_2$ and analysis of the normal states of the $R(T)$ profiles. (a) Left y axis: CDW transition temperature T_{CDW}. The solid curves are the fitting results by the mean-field power law, $T_{CDW}(P) = T_0(1 - P/P_c)^{\beta}$. Right y axis: superconducting transition temperature T_c. (b) The pressure-dependent fitted parameters exponent n (left y axis), and A (right y axis), respectively.

enhancement of superconductivity is caused by the suppression of ICCDW in the *H*-layer below 1.1 GPa, while the further enhanced superconductivity and the SC dome are related to the suppression and the possible quantum fluctuation of the CCDW order in the *T*-layer. This is understandable because the CCDW of the *T*-layer is three-dimensional (3D) while the ICCDW in the *H*-layer is 2D.[9,10,34] The out-of-plane displacements of "star of David" clusters in the CCDW phase cause a periodic swelling of the *T*-layer.[9,10] Thus, the suppression of the CCDW in the *T*-layer would also influence the superconductivity of the adjacent *H*-layer.

A pressure-induced structural phase transition (SPT) from a layered quasi-2D to a 3D crystal structure has been reported recently for 1*T*-TaS_2 and 2*H*-TaS_2 bulk samples,[17,19] and their structural evolutions were closely related to superconductivity. To check whether the new superconductivity in our 4*Hb*-$TaSe_2$ system was induced by SPT, we performed in situ high-pressure XRD measurements. Figure 3a shows the selected XRD patterns between 1.5 and 40.8 GPa. All representative diffraction peaks shifted to high angles during compression, and no new peaks were observed, indicating that 4*Hb*-$TaSe_2$ retains its ambient crystallographic symmetry, which rules out a SPT as the origin of the emergent higher-T_c superconductivity. However, the Bragg peaks are broadened after ∼20 GPa (Figure 3a and Figure S7a,b). We have carefully analyzed the full width at half-maximum (FWHM) and the Bragg peak center positions by fitting the intensity profiles of representative Bragg peaks (004) and (104) with the Gaussian model. As shown in Figures S7c,d, both the $2\theta(P)$ and FWHM(P) profiles show obvious changes at ∼10.0 and ∼20.0 GPa. Considering that no SPT occurs in compressed 4*Hb*-$TaSe_2$, these anomalous behaviors of Bragg peaks may imply an isostructural phase transition (iSPT). Then, we extracted the structural parameters (including lattice parameters, bond length, and unit cell volume) by a structural refinement

https://doi.org/10.1021/acs.nanolett.2c04385
Nano Lett. 2023, 23, 2121−2128

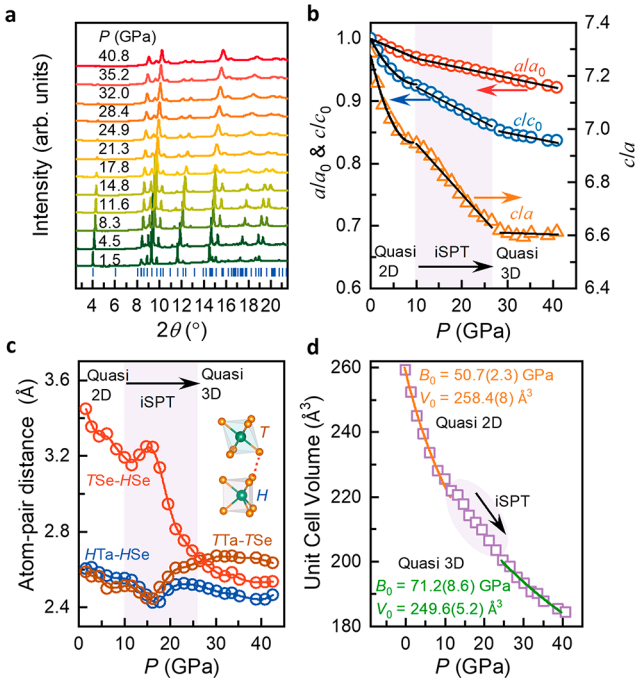

Figure 3. Synchrotron XRD and structure evolution of 4*Hb*-$TaSe_2$ at high pressure. (a) Representative powder XRD patterns between 1.5 and 40.8 GPa (run 1). (b) Pressure-dependent normalized compression ratios a/a_0 and c/c_0 (left) and c/a (right) extracted from powder diffraction Rietveld refinements. The solid lines are guides for the eyes. (c) Interlayer Se−Se distance and Ta−Se bond length in the *H*- and *T*-layers as a function of pressure. The solid lines and light purple shades are guides for the eyes. (d) Pressure-dependent unit-cell volume. Solid lines are the fitting curves with the Birch−Murnaghan equation of state.[38]

analysis of the XRD patterns from ambient pressure to the highest pressure of 40.8 GPa. Representative refinement profiles are plotted in Figure S8. As shown in Figure 3b, compared to the near-continuous compression of normalized lattice a/a_0, c/c_0 presents a clear three-stage compression behavior: a fast shrinkage for 0 GPa ≤ P ≤ 10.0 GPa followed by two different linear compression rates for 10.0 GPa ≤ P ≤ 26.0 GPa and 26.0 GPa ≤ P ≤ 40.8 GPa. The c/a ratio (Figure 3b, right) also shares a similar three-stage behavior. The discontinuities of the pressure-dependent lattice parameters have also been reported for other TMDs (such as 1*T*-$TiTe_2$).[39] And the nearly pressure-independent c/a ratios in Figure 3b have also been observed in 1*T*-$TiTe_2$, which signifies a transformation from an anisotropic quasi-2D to an isotropic quasi-3D structure.[39]

To explore whether the layered nature is maintained or not at high pressure, we further extracted the interlayer Se−Se distance and intralayer Ta−Se bond length as a function of pressure; the results are presented in Figure 3c. The interlayer Se−Se distance between the *T*- and *H*-layers tends to form a peak for 10.0 GPa ≤ P ≤ 26.0 GPa, which is in marked contrast to "valleys" of the intralayer Ta−Se bond length in the *H*-layer and *T*-layer (also see Figure S9 for the layer-dependent compression behavior and the distortion of the geometric ligands). Such a strong competing correlation between the interlayer Se−Se distance and intralayer Ta−Se bond length implies the occurrence of iSPT upon compression, which consequently leads to the compression anomalies of the c/a ratio at 10.0 GPa. Above 26.0 GPa, the compressed interlayer Se−Se distance is comparable to the intralayer Ta−Se bond length in either the *T*-layer or *H*-layer, which further confirms the formation of a quasi-3D structure. It should be noted that 4*Hb*-$TaSe_2$ still maintains its layered nature because the

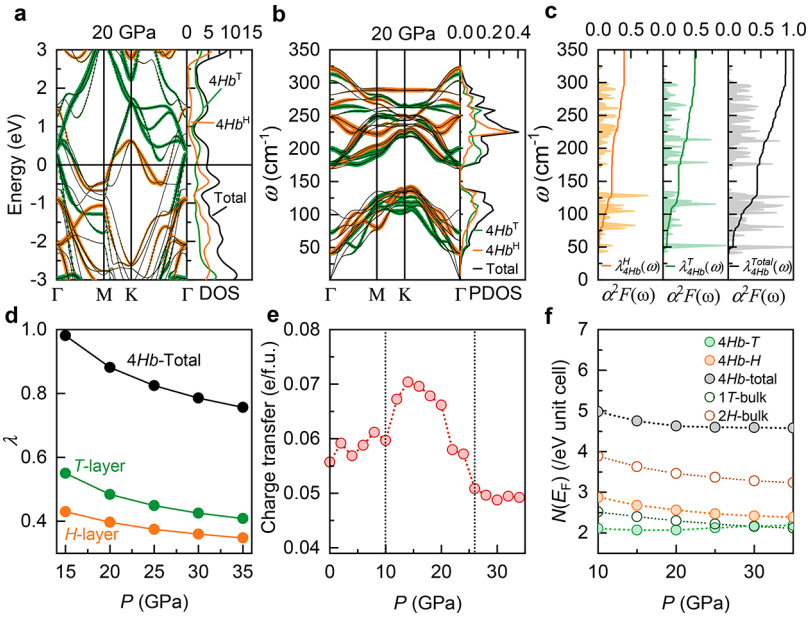

Figure 4. Calculated band structures, phonon dispersions, and EPC of 4*Hb*-$TaSe_2$. (a) The left panel shows the projected band structures of the *H*-layer (orange) and *T*-layer (green) at 20 GPa. The right panel presents the projected electronic density of states (DOS) in states/eV unit cell. (b) Projected phonon dispersions and PDOS of the *H*-layer and *T*-layer at 20 GPa, revealing well-separated low-frequency (below 150 cm^{-1}) and high-frequency (above 150 cm^{-1}) phonon branches. (c) The individual Eliashberg spectral function $\alpha^2F(\omega)$ and accumulated frequency-dependent EPC constants are projected to the *H*- and *T*-layers at 20 GPa. (d) The pressure-dependent EPC constant λ and its projections to the *T*-layer and *H*-layer between 15 and 35 GPa. (e) The pressure-dependent charge transfer from the *T*-layer to the *H*-layer. The dashed lines are guides for the eyes. (f) Density of states at the Fermi level $N(E_F)$ as a function of pressure.

https://doi.org/10.1021/acs.nanolett.2c04385
Nano Lett. 2023, 23, 2121−2128

interlayer Se−Se distance of 2.6 Å at the highest pressure of 40.8 GPa in this work has not reached the Se atoms' covalent bond length (2.3 Å),[40] as shown in Figure 3c. As shown in Figure 3d, the fitting with the second-order (B_0' = 4.0) Birch−Murnaghan equation of state[38] yields bulk moduli of B_0 = 50.7(2.3) GPa and V_0 = 258.4(8) Å^3 in the quasi-2D region (0 GPa < P < 10.0 GPa) and B_0= 71.2(8.6) GPa and V_0 = 249.6(5.2) Å^3 in the quasi-3D region (26.0 GPa < P < 40.8 GPa). A second run of high-pressure XRD (Figure S10) and Raman-scattering measurements (Figure S11) undoubtedly confirms the iSPT of 4*Hb*-$TaSe_2$ at ∼10 GPa and the transition from quasi-2D to quasi-3D at above 26 GPa. This iSPT is reversible after fully releasing the applied pressure (see Figures S10 and S11 in the Supporting Information).

Electronic band structure calculations (Figures S12 and S13) show that there is no pressure-induced topological change at the Fermi surface. The structural relaxation calculations suggest that the CCDW in the *T*-layer disappears at 10 GPa (Figure S14). The experimental electrical transport measurements confirm the missing signature of the CCDW in the *T*-layer at 3.2 GPa and above (Figure 1c); thus, one could expect that the long-range CCDW order transforms to a short-range order and the latter may survive until ∼10 GPa. With this consideration, we calculated the projected phonon spectra and EPC strengths from 15 to 35 GPa without CDW influence. As a representative, the individual projections of the band structure and phonon dispersion to the *H*-layer and *T*-layer at 20 GPa are presented in Figures 4a,b, respectively. The Eliashberg spectral function $\alpha^2F(\omega)$ and the accumulated frequency-dependent EPC constants $\lambda(\omega)$ are plotted in Figure 4c. It can be seen that the low-frequency and high-frequency phonon branches make almost equal contributions to the total λ. At 20 GPa, the total λ is ∼0.88. On projection into the individual layer, the λ of the *T*-layer (∼0.48) is higher than that of the *H*-layer (∼0.4). Figure 4d depicts the evolution of the total λ and its layer-dependent projection between 15 and 35 GPa. The result demonstrates that the EPC strength from the *T*-layer is always stronger than that of the *H*-layer, resulting in a higher T_c from the *T*-layer (Figure S15). The projected EPC constant in phonon dispersions at 20.0 GPa is displayed in Figure S16.

We also calculated the Bader charge to estimate the charge transfer between the *T*-layer and the *H*-layer in 4*Hb*-$TaSe_2$ (see Figure 4e). It shows 0.055 electron per $TaSe_2$ formula unit (e/f.u.) transfers from the *T*-layer to the *H*-layer at ambient pressure, to equalize the two Fermi levels of the *H*-layer and *T*-layer in forming 4*Hb*-$TaSe_2$.[34,41,42] When applying pressure, the charge transfer slightly increases by 0.005 e/f.u. until 10 GPa, together with the quasi-2D nature of the compression character discussed previously with the XRD probe, indicating that the interlayer coupling is very weak. However, the charge transfer shows an abnormal increase at 10 GPa and reaches a maximum of 0.07 e/f.u. at 14 GPa, followed by a rapid decrease with pressure and remains at the lowest value of ∼0.05 e/f.u. beyond 26 GPa, where 4*Hb*-$TaSe_2$ transforms to a quasi-3D structure, consistent with the XRD result.

Furthermore, for the dual-layer superconductivity (>9.6 GPa), the T_c value of the *H*-layer within 4*Hb*-$TaSe_2$ is lower than that of the bulk 2*H*-$TaSe_2$,[15] while the superconductivity of the *T*-layer is almost invariable compared to bulk 1*T*-$TaSe_2$ (although the superconductivity enters at different pressures for 4*Hb*-$TaSe_2$ (9.6 GPa) and bulk 1*T*-$TaSe_2$ (4.5 GPa)).[16] According to previous works, the charge transfer may result in the modulation of DOS at the Fermi level ($N(E_F)$).[43,44] Consequently, the superconductivity would be influenced by the change of $N(E_F)$ according to the Bardeen−Cooper−Schrieffer (BCS) theory ($T_c \propto N(E_F)$).[45] Thus, we further calculated the $N(E_F)$ values of the *T*-layer, *H*-layer (within 4*Hb*-$TaSe_2$), and their bulk counterparts in the pressure range of 10−35 GPa. As shown in Figure 4f, $N(E_F)$ of the *H*-layer is significantly decreased compared to that of the bulk 2*H*-$TaSe_2$, while $N(E_F)$ of the *T*-layer is almost in line with that of the bulk 1*T*-$TaSe_2$. This can be explained by the different shapes of the DOS of the *T*(*H*)-layer near the Fermi level: a rather flat DOS shape of the *T*-layer and a sharp peak of the *H*-layer near the Fermi level (Figure 4a). Consequently, the shift of the band induced by the charge transfer cannot pronouncedly change $N(E_F)$ of the *T*-layer, in stark contrast to the *H*-layer. Thus, the superconductivity of the *H*-layer is more sensitive to interlayer coupling than the *T*-layer.

In summary, we comprehensively investigated the interplay between the CDW and SC in a natural 4*Hb*-$TaSe_2$ heterostructure, which consists of alternately stacking 1*H*- and 1*T*-layers. Under high pressure, we observed both CDWs and SC from individual layers and a competing relationship among the CDWs and SC. The suppression of the CDW boosts SC not only in its layer but also within the adjacent layer. Furthermore, dual-layer superconductivity emerges when both CDW orders collapse. The different phase diagrams from the *H*- and *T*-layers in 4*Hb*-$TaSe_2$ and the noticeable differences between them and their bulk counterparts reveal that the electronic properties are largely dependent on the structural configurations. The special competing relationship and dual-layer superconductivity reported here for the first time in TMD VDWHs provides crucial guidance for the application of devices based on VDWHs and offers a new direction to deepen our understanding of this interesting class of materials.

■ ASSOCIATED CONTENT

Supporting Information

The Supporting Information is available free of charge at https://pubs.acs.org/doi/10.1021/acs.nanolett.2c04385.

Materials and methods, preparation of 4*Hb*-$TaSe_2$ and characterization, electrical transport measurements, high-pressure XRD and Raman scattering measurements, and first-principles calculations (PDF)

■ AUTHOR INFORMATION

Corresponding Authors

Jian Sun − *National Laboratory of Solid State Microstructures, School of Physics and Collaborative Innovation Center of Advanced Microstructures, Nanjing University, Nanjing 210093, People's Republic of China;* orcid.org/0000-0001-6172-9100; Email: jiansun@nju.edu.cn

Xin Wang − *State Key Laboratory of Superhard Materials, Department of Physics, Jilin University, Changchun 130012, People's Republic of China*; Email: xin_wang@jlu.edu.cn

Wenge Yang − *Center for High Pressure Science and Technology Advanced Research, Shanghai 201203, People's Republic of China;* orcid.org/0000-0001-8436-8731; Email: yangwg@hpstar.ac.cn

https://doi.org/10.1021/acs.nanolett.2c04385
Nano Lett. 2023, 23, 2121−2128

Authors

Limin Yan − *State Key Laboratory of Superhard Materials, Department of Physics, Jilin University, Changchun 130012, People's Republic of China; Center for High Pressure Science and Technology Advanced Research, Shanghai 201203, People's Republic of China*

Chi Ding − *National Laboratory of Solid State Microstructures, School of Physics and Collaborative Innovation Center of Advanced Microstructures, Nanjing University, Nanjing 210093, People's Republic of China*

Mingtao Li − *Center for High Pressure Science and Technology Advanced Research, Shanghai 201203, People's Republic of China*

Ruilian Tang − *School of Materials Science and Engineering, Changchun University of Science and Technology, Changchun 130022, People's Republic of China*

Wan Chen − *State Key Laboratory of Superhard Materials, Department of Physics, Jilin University, Changchun 130012, People's Republic of China*

Bingyan Liu − *Center for High Pressure Science and Technology Advanced Research, Shanghai 201203, People's Republic of China*

Kejun Bu − *Center for High Pressure Science and Technology Advanced Research, Shanghai 201203, People's Republic of China;* orcid.org/0000-0002-1466-2764

Tianheng Huang − *National Laboratory of Solid State Microstructures, School of Physics and Collaborative Innovation Center of Advanced Microstructures, Nanjing University, Nanjing 210093, People's Republic of China*

Dongzhe Dai − *State Key Laboratory of Surface Physics, Department of Physics, Fudan University, Shanghai 200438, People's Republic of China*

Xiaobo Jin − *State Key Laboratory of Surface Physics, Department of Physics, Fudan University, Shanghai 200438, People's Republic of China*

Xiaofan Yang − *State Key Laboratory of Surface Physics, Department of Physics, Fudan University, Shanghai 200438, People's Republic of China*

Erjian Cheng − *State Key Laboratory of Surface Physics, Department of Physics, Fudan University, Shanghai 200438, People's Republic of China*

Nana Li − *Center for High Pressure Science and Technology Advanced Research, Shanghai 201203, People's Republic of China*

Qian Zhang − *Center for High Pressure Science and Technology Advanced Research, Shanghai 201203, People's Republic of China*

Fengliang Liu − *Center for High Pressure Science and Technology Advanced Research, Shanghai 201203, People's Republic of China*

Xuqiang Liu − *Center for High Pressure Science and Technology Advanced Research, Shanghai 201203, People's Republic of China*

Dongzhou Zhang − *Hawaii Institute of Geophysics & Planetology, University of Hawaii Manoa, Honolulu, Hawaii 96822, United States;* orcid.org/0000-0002-6679-892X

Shuailing Ma − *State Key Laboratory of Superhard Materials, Department of Physics, Jilin University, Changchun 130012, People's Republic of China*

Qiang Tao − *State Key Laboratory of Superhard Materials, Department of Physics, Jilin University, Changchun 130012, People's Republic of China;* orcid.org/0000-0002-6357-5552

Pinwen Zhu − *State Key Laboratory of Superhard Materials, Department of Physics, Jilin University, Changchun 130012, People's Republic of China*

Shiyan Li − *State Key Laboratory of Surface Physics, Department of Physics, Fudan University, Shanghai 200438, People's Republic of China*

Xujie Lü − *Center for High Pressure Science and Technology Advanced Research, Shanghai 201203, People's Republic of China;* orcid.org/0000-0001-8402-7160

Complete contact information is available at: https://pubs.acs.org/10.1021/acs.nanolett.2c04385

Author Contributions

W.Y. and X.W. conceived and designed the project. L.Y. performed the synthesis and high-pressure Raman and transport measurements. W.C., S.M., Q.T., and P.Z. helped to synthesize the experimental single crystals. R.T., B.L., N.L., Q.Z., X.L., D.Z., and X.L.. assisted with conducting the high-pressure XRD measurements. M.L., D.D., X.J., X.Y., E.C., S.L., N.L., and F.L. assisted with the transport measurements. C.D., T.H., and J.S. performed the DFT calculations. L.Y., C.D., M.L., and K.B. analyzed the data and wrote the original manuscript. All authors contributed to the discussion of the results and revision of the manuscript. L.Y. and C.D. contributed equally to this work.

Funding

This work was supported by the National Natural Science Foundation of China under Grants No. U1930401, 11804011, 11974162, 11834006, 12125404, and 12104065 and the Fundamental Research Funds for the Central Universities. J.S. gratefully acknowledges the financial support from the National Key R&D Program of China (grant nos. 2022YFA1403201).

Notes

The authors declare no competing financial interest.

■ ACKNOWLEDGMENTS

In situ high-pressure X-ray diffraction measurements were performed at Sector 13, Advanced Photon Source (APS), Argonne National Laboratory. GeoSoilEnviroCARS is supported by the National Science Foundation-Earth Sciences (EAR-1634415) and the Department of Energy-GeoSciences (DE-FG02-94ER14466). The Advanced Photon Source, a U.S. Department of Energy (DOE) Office of Science User Facility, is operated for the DOE Office of Science by Argonne National Laboratory under Contract No. DE-AC02-06CH11357. Partial XRD work was completed at the 15U1 station, Shanghai Synchrotron Radiation Facility (SSRF), Zhangjiang Lab, and the BL10-XU station at Spring-8. We appreciate the technical support of Drs. S. Jiang, S. Kawaguchi, and Y. Ohishi. The calculations were carried out using supercomputers at the High Performance Computing Center of Collaborative Innovation Center of Advanced Microstructures, the high-performance supercomputing center of Nanjing University. The authors appreciate Ms. Freyja O'Toole for language editing. The authors acknowledge the financial support from Shanghai Science and Technology Committee, China (No. 22JC1410300) and Shanghai Key Laboratory of Material Frontiers Research in Extreme Environments, China (No. 22dz2260800).

■ ABBREVIATIONS

2D, two-dimensional; VDWHs, van der Waals heterostructures; TMD, transition-metal dichalcogenide; CDW, charge-density wave; SC, superconductivity; EPC, electron−phonon coupling; HTHP, high temperature and high pressure; DOS, density of states; ICCDW, incommensurate charge-density wave; CCDW, commensurate charge-density wave; SPT, structural phase transition; and iSPT, isostructural phase transition

■ REFERENCES

(1) Geim, A. K.; Grigorieva, I. V. Van der Waals heterostructures. *Nature* **2013**, *499*, 419.

(2) Liu, Y.; Weiss, N. O.; Duan, X.; Cheng, H.-C.; Huang, Y.; Duan, X. Van der Waals heterostructures and devices. *Nat. Rev. Mater.* **2016**, *1* (9), 16042.

(3) Novoselov, K. S.; Mishchenko, A.; Carvalho, A.; Castro Neto, A. H. 2D materials and van der Waals heterostructures. *Science* **2016**, *353* (6298), aac9439.

(4) Kezilebieke, S.; Huda, M. N.; Vaňo, V.; Aapro, M.; Ganguli, S. C.; Silveira, O. J.; Głodzik, S.; Foster, A. S.; Ojanen, T.; Liljeroth, P. Topological superconductivity in a van der Waals heterostructure. *Nature* **2020**, *588* (7838), 424−428.

(5) Chen, Y.; Wu, L.; Xu, H.; Cong, C.; Li, S.; Feng, S.; Zhang, H.; Zou, C.; Shang, J.; Yang, S. A.; Loh, K. P.; Huang, W.; Yu, T. Visualizing the Anomalous Charge Density Wave States in Graphene/$NbSe_2$ Heterostructures. *Adv. Mater.* **2020**, *32* (45), 2003746.

(6) Zhao, W.-M.; Zhu, L.; Nie, Z.; Li, Q.-Y.; Wang, Q.-W.; Dou, L.-G.; Hu, J.-G.; Xian, L.; Meng, S.; Li, S.-C. Moiré enhanced charge density wave state in twisted 1*T*-$TiTe_2$/1*T*-$TiSe_2$ heterostructures. *Nat. Mater.* **2022**, *21* (3), 284−289.

(7) Qiu, X.-L.; Zhang, J.-F.; Gong, B.-C.; Yang, H.-C.; Lu, Z.-Y.; Liu, K. Modulating charge density wave states in $TaSe_2$ by an electride substrate. *Phys. Rev. B* **2021**, *104* (16), 165109.

(8) Wang, Z.; Chu, L.; Li, L.; Yang, M.; Wang, J.; Eda, G.; Loh, K. P. Modulating Charge Density Wave Order in a 1*T*-TaS_2/Black Phosphorus Heterostructure. *Nano Lett.* **2019**, *19* (5), 2840−2849.

(9) Ji, S.; Grånäs, O.; Rossnagel, K.; Weissenrieder, J. Transient three-dimensional structural dynamics in 1*T*-$TaSe_2$. *Phys. Rev. B* **2020**, *101* (9), 094303.

(10) Bovet, M.; van Smaalen, S.; Berger, H.; Gaal, R.; Forró, L.; Schlapbach, L.; Aebi, P. Interplane coupling in the quasi-two-dimensional 1*T*-TaS_2. *Phys. Rev. B* **2003**, *67* (12), 125105.

(11) Morosan, E.; Zandbergen, H. W.; Dennis, B. S.; Bos, J. W. G.; Onose, Y.; Klimczuk, T.; Ramirez, A. P.; Ong, N. P.; Cava, R. J. Superconductivity in Cu_xTiSe_2. *Nat. Phys.* **2006**, *2*, 544.

(12) Li, L.; Deng, X.; Wang, Z.; Liu, Y.; Abeykoon, M.; Dooryhee, E.; Tomic, A.; Huang, Y.; Warren, J. B.; Bozin, E. S.; Billinge, S. J. L.; Sun, Y.; Zhu, Y.; Kotliar, G.; Petrovic, C. Superconducting order from disorder in 2*H*-$TaSe_{2-x}S_x$. *npj Quantum Mater.* **2017**, *2* (1), 11.

(13) Wang, B.; Liu, Y.; Luo, X.; Ishigaki, K.; Matsubayashi, K.; Lu, W.; Sun, Y.; Cheng, J.; Uwatoko, Y. Universal phase diagram of superconductivity and charge density wave versus high hydrostatic pressure in pure and Se-doped 1*T*-TaS_2. *Phys. Rev. B* **2018**, *97* (22), 220504.

(14) Kusmartseva, A. F.; Sipos, B.; Berger, H.; Forró, L.; Tutiš, E. Pressure Induced Superconductivity in Pristine 1*T*-$TiSe_2$. *Phys. Rev. Lett.* **2009**, *103* (23), 236401.

(15) Freitas, D. C.; Rodière, P.; Osorio, M. R.; Navarro-Moratalla, E.; Nemes, N. M.; Tissen, V. G.; Cario, L.; Coronado, E.; García-Hernández, M.; Vieira, S.; Núñez-Regueiro, M.; Suderow, H. Strong enhancement of superconductivity at high pressures within the charge-density-wave states of 2*H*-TaS_2 and 2*H*-$TaSe_2$. *Phys. Rev. B* **2016**, *93* (18), 184512.

(16) Wang, B.; Liu, Y.; Ishigaki, K.; Matsubayashi, K.; Cheng, J.; Lu, W.; Sun, Y.; Uwatoko, Y. Pressure-induced bulk superconductivity in a layered transition-metal dichalcogenide 1*T*-tantalum selenium. *Phys. Rev. B* **2017**, *95* (22), 220501.

(17) Dong, Q.; Li, Q.; Li, S.; Shi, X.; Niu, S.; Liu, S.; Liu, R.; Liu, B.; Luo, X.; Si, J.; Lu, W.; Hao, N.; Sun, Y.; Liu, B. Structural phase transition and superconductivity hierarchy in 1*T*-TaS_2 under pressure up to 100 GPa. *npj Quantum Mater.* **2021**, *6* (1), 20.

(18) Xu, S.; Gao, J.; Liu, Z.; Chen, K.; Yang, P.; Tian, S.; Gong, C.; Sun, J.; Xue, M.; Gouchi, J.; Luo, X.; Sun, Y.; Uwatoko, Y.; Lei, H.; Wang, B.; Cheng, J. Effects of disorder and hydrostatic pressure on charge density wave and superconductivity in 2*H*-TaS_2. *Phys. Rev. B* **2021**, *103* (22), 224509.

(19) Dong, Q.; Pan, J.; Li, S.; Fang, Y.; Lin, T.; Liu, S.; Liu, B.; Li, Q.; Huang, F.; Liu, B. Record-High Superconductivity in Transition Metal Dichalcogenides Emerged in Compressed 2*H*-TaS_2. *Adv. Mater.* **2022**, *34* (9), 2103168.

(20) Sipos, B.; Kusmartseva, A. F.; Akrap, A.; Berger, H.; Forró, L.; Tutiš, E. From Mott state to superconductivity in 1*T*-TaS_2. *Nat. Mater.* **2008**, *7* (12), 960−965.

(21) Rice, T. M.; Scott, G. K. New Mechanism for a Charge-Density-Wave Instability. *Phys. Rev. Lett.* **1975**, *35* (2), 120−123.

(22) Ke, F.; Chen, Y.; Yin, K.; Yan, J.; Zhang, H.; Liu, Z.; Tse, J. S.; Wu, J.; Mao, H.-k.; Chen, B. Large bandgap of pressurized trilayer graphene. *Proc. Natl. Acad. Sci. U.S.A.* **2019**, *116* (19), 9186.

(23) Ribak, A.; Skiff, R. M.; Mograbi, M.; Rout, P. K.; Fischer, M. H.; Ruhman, J.; Chashka, K.; Dagan, Y.; Kanigel, A. Chiral superconductivity in the alternate stacking compound 4*Hb*-TaS_2. *Sci. Adv.* **2020**, *6* (13), 6.

(24) Gao, J. J.; Si, J. G.; Luo, X.; Yan, J.; Jiang, Z. Z.; Wang, W.; Han, Y. Y.; Tong, P.; Song, W. H.; Zhu, X. B.; Li, Q. J.; Lu, W. J.; Sun, Y. P. Origin of the large magnetoresistance in the candidate chiral superconductor 4*Hb*-TaS_2. *Phys. Rev. B* **2020**, *102* (7), 075138.

(25) Wen, C.; Gao, J.; Xie, Y.; Zhang, Q.; Kong, P.; Wang, J.; Jiang, Y.; Luo, X.; Li, J.; Lu, W.; Sun, Y.-P.; Yan, S. Roles of the Narrow Electronic Band near the Fermi Level in 1*T*-TaS_2-Related Layered Materials. *Phys. Rev. Lett.* **2021**, *126* (25), 256402.

(26) Shen, S.; Qin, T.; Gao, J.; Wen, C.; Wang, J.; Wang, W.; Li, J.; Luo, X.; Lu, W.; Sun, Y.; Yan, S. Coexistence of Quasi-two-dimensional Superconductivity and Tunable Kondo Lattice in a van der Waals Superconductor. *Chin. Phys. Lett.* **2022**, *39* (7), 077401.

(27) Achari, A.; Bekaert, J.; Sreepal, V.; Orekhov, A.; Kumaravadivel, P.; Kim, M.; Gauquelin, N.; Balakrishna Pillai, P.; Verbeeck, J.; Peeters, F. M.; Geim, A. K.; Milošević, M. V.; Nair, R. R. Alternating Superconducting and Charge Density Wave Monolayers within Bulk 6*R*-TaS_2. *Nano Lett.* **2022**, *22* (15), 6268−6275.

(28) Xia, J.; Yan, J.; Wang, Z.; He, Y.; Gong, Y.; Chen, W.; Sum, T. C.; Liu, Z.; Ajayan, P. M.; Shen, Z. Strong coupling and pressure engineering in WSe_2-$MoSe_2$ heterobilayers. *Nat. Phys.* **2021**, *17* (1), 92−98.

(29) Pandey, T.; Nayak, A. P.; Liu, J.; Moran, S. T.; Kim, J.-S.; Li, L.-J.; Lin, J.-F.; Akinwande, D.; Singh, A. K. Pressure-Induced Charge Transfer Doping of Monolayer Graphene/MoS_2 Heterostructure. *Small* **2016**, *12* (30), 4063−4069.

(30) Bjerkelund, E.; Kjekshus, A.; et al. On the structural properties of $Ta_{1+x}Se_2$ phase. *Acta Chem. Scand.* **1967**, *21*, 513.

(31) Lian, C.-S.; Heil, C.; Liu, X.; Si, C.; Giustino, F.; Duan, W. Coexistence of Superconductivity with Enhanced Charge Density Wave Order in the Two-Dimensional Limit of $TaSe_2$. *J. Phys. Chem. Lett.* **2019**, *10* (14), 4076−4081.

(32) Kumakura, T.; Tan, H.; Handa, T.; Morishita, M.; Fukuyama, H. Charge density waves and superconductivity in 2*H*-$TaSe_2$. *Czech. J. Phys.* **1996**, *46* (5), 2611−2612.

(33) Yokota, K.-i.; Kurata, G.; Matsui, T.; Fukuyama, H. Superconductivity in the quasi-two-dimensional conductor 2*H*-$TaSe_2$. *Physica B: Condensed Matter* **2000**, *284*−*288*, 551−552.

(34) Di Salvo, F. J.; Moncton, D. E.; Wilson, J. A.; Mahajan, S. Coexistence of two charge-density waves of different symmetry in 4*Hb*-$TaSe_2$. *Phys. Rev. B* **1976**, *14* (4), 1543−1546.

https://doi.org/10.1021/acs.nanolett.2c04385
Nano Lett. 2023, 23, 2121−2128

(35) Woollam, J. A.; Somoano, R. B.; O'Connor, P. Positive Curvature of the H_{c2}-versus-T_c Boundaries in Layered Superconductors. *Phys. Rev. Lett.* **1974**, *32* (13), 712−714.
(36) Joe, Y. I.; Chen, X. M.; Ghaemi, P.; Finkelstein, K. D.; de la Pena, G. A.; Gan, Y.; Lee, J. C. T.; Yuan, S.; Geck, J.; MacDougall, G. J.; Chiang, T. C.; Cooper, S. L.; Fradkin, E.; Abbamonte, P. Emergence of charge density wave domain walls above the superconducting dome in 1*T*-$TiSe_2$. *Nat. Phys.* **2014**, *10* (6), 421−425.
(37) Chu, C. W.; Testardi, L. R.; Di Salvo, F. J.; Moncton, D. E. Pressure effects on the charge-density-wave phases in 2*H*-$TaSe_2$. *Phys. Rev. B* **1976**, *14* (2), 464−467.
(38) Birch, F. Finite Elastic Strain of Cubic Crystals. *Phys. Rev.* **1947**, *71* (11), 809−824.
(39) Rajaji, V.; Dutta, U.; Sreeparvathy, P. C.; Sarma, S. C.; Sorb, Y. A.; Joseph, B.; Sahoo, S.; Peter, S. C.; Kanchana, V.; Narayana, C. Structural, vibrational, and electrical properties of 1*T*-$TiTe_2$ under hydrostatic pressure: Experiments and theory. *Phys. Rev. B* **2018**, *97* (8), 085107.
(40) Bremholm, M.; Hor, Y. S.; Cava, R. J. Pressure stabilized Se−Se dimer formation in $PbSe_2$. *Solid State Sci.* **2011**, *13* (1), 38−41.
(41) Friend, R. H.; Frindt, R. F.; Grant, A. J.; Yoffe, A. D.; Jerome, D. Electrical conductivity and charge density wave formation in 4*Hb*-TaS_2 under pressure. *J. Phys. C: Solid State Phys.* **1977**, *10* (7), 1013.
(42) Nakashizu, T.; Sekine, T.; Uchinokura, K.; Matsuura, E. Raman Study of Charge-Density-Wave Phase Transitions in 4*Hb*-$TaSe_2$. *J. Phys. Soc. Jpn.* **1986**, *55* (2), 672−682.
(43) Yao, Q.; Shen, D. W.; Wen, C. H. P.; Hua, C. Q.; Zhang, L. Q.; Wang, N. Z.; Niu, X. H.; Chen, Q. Y.; Dudin, P.; Lu, Y. H.; Zheng, Y.; Chen, X. H.; Wan, X. G.; Feng, D. L. Charge Transfer Effects in Naturally Occurring van der Waals Heterostructures $(PbSe)_{1.16}(TiSe_2)_m$(m = 1, 2). *Phys. Rev. Lett.* **2018**, *120* (10), 106401.
(44) Che, L.; Le, T.; Huang, Q.; Yin, L.; Chen, Y.; Yang, X.; Xu, Z.-A.; Lu, X. Point-contact Andreev reflection spectroscopy on the misfit phase superconductors $PbSe_{1.12}TaSe_2$ doped with Cl or Br. *Phys. Rev. B* **2019**, *99* (2), 024512.
(45) Bardeen, J.; Cooper, L. N.; Schrieffer, J. R. Theory of Superconductivity. *Phys. Rev. B* **1957**, *108* (5), 1175−1204.

https://doi.org/10.1021/acs.nanolett.2c04385
Nano Lett. 2023, 23, 2121−2128